



Photocatalytic Degradation of Congo Red Dye via Multi-Walled Carbon Nanotubes Modified CuO and ZnO Nanoparticles under Visible Light Irradiation

Amal Abdel-Fatah Alkahlawy*, Radwa Abbas El-Salamony, Heba Mahmoud Gobara



CrossMark

Egyptian Petroleum Research Institute (EPRI), 1 Ahmed El-Zomor Street, Nasr City, 11727 Cairo, Egypt.

Abstract

The photocatalytic degradation of congo red dye (CR) using nanocomposites materials of multi-walled carbon nanotubes combined with some transition metal oxide under visible light irradiation was studied. Multi-walled carbon nanotubes were prepared via chemical vapour synthesis (CVS) and loaded with some transition elements as Cu, Zn, and $\text{Cu}_{0.1}\text{Zn}_{0.9}\text{O}$ nanoparticles, where the ratio of metal was kept constant in all catalysts (20% M). Various Characteristic techniques were adopted such as X-Ray Diffraction (XRD), Nitrogen adsorption-desorption, Transmission Electron Microscope (TEM), Fourier Transform Infra-Red (FT-IR), Ultra Violet reflectance analysis (UV), Scanning Electron Microscope (SEM), Energy dispersive X-ray Spectroscopy (EDX), Photoluminescence (PL) spectroscopy and Raman spectroscopy. The results proved that the mother carbon nanotubes have a high surface area and total pore volume and are found to be $247\text{m}^2/\text{g}$ and $0.569\text{cm}^3/\text{g}$, respectively, and its surface area decreased upon loading the metal nanoparticles. Pore size distribution curve (PSD) exhibited a wide mesopore centered at 30 nm. TEM results revealed that Cu and Zn metals are randomly distributed and located at the nanotube's surface and the tips of the tube via the tip-growth mechanism. It is seen that the Zn/CNTs have a homogeneously uniform diameter as compared to the neat CNTs. The nanocomposites' photodegradation% rank was Zn/CNT > Cu/CNT > Cu-Zn/CNT, which related mainly to the chemical composition of Zn/CNT composite. Zn/CNT composite showed the highest degradation efficiency among the prepared composites, which achieved 97.7% after 70 minutes under visible light irradiation. The mechanism of the photocatalytic degradation of congo red dye under visible light irradiation was discussed.

Keywords: Composites materials; Congo Red Dye; Nano-materials; Photocatalytic degradation

1. Introduction

Nanoscience and nanotechnology are considered to have huge potential to bring benefits to many areas of research and application and are attracting rapidly increasing [1]. Transition metal NPs can be seen to be very desirable to employ like catalysts because of their massive ratio of surface to volume and great energy at the surface, making the atoms of their surface very useful [2–4]. Metal NPs represent a powerful catalyst for a whole range of reactions, such as C–C coupling, hydrogenation, and oxidation reactions [5]. Metal oxide (NPs) are promising substances since they could be synthesized with a relatively high surface area and highly ionic, with

unique crystallography that could show many surface reaction sites [6].

Semiconductor photocatalysis technology, which can provide active solar energy, is a promising method for water pollution treatment [7]. CuO and ZnO NPs based photocatalyst is the most commonly used material in wastewater treatment [8–10]. Due to its high chemical stability, low cost, and relatively high quantum efficiency, ZnO can be considered a relative photocatalyst. ZnO nanoparticles are active only in the UV range and showed a medium performance. CuO is often utilized as a cocatalyst due to its low energy gap. The combination of CuO with comprehensive band gap catalysts such as TiO_2 or ZnO leads to an increase in the photocatalytic rate

*Corresponding author e-mail: amal_kahlawy@yahoo.com; (Amal Abdel-Fatah Alkahlawy).

Receive Date: 29 October 2020, Revised Date: 22 November 2020, Accept Date: 29 November 2020.

DOI: 10.21608/EJCHEM.2020.47684.2985

©2021 National Information and Documentation Center (NIDOC)

under visible light. It has been demonstrated that CuO/ZnO nanocomposites exhibit improved charge carrier separation and decreased the rate of hole-electron recombination, which improves photo-degradation efficiency [11]. A significant effort has been made to develop supported semiconductors that demand a high effective surface area and respond to visible light just as simple removal and separation from water [12–16].

Among these supports, carbon nanotubes (CNTs), individuals from structural fullerene groups, have been incredibly crucial between the scientists were their first detection [17,18]. CNTs have a massive measure of the market potential in different fields such as microscopes, chemical, and biological sciences, nano-mechanics, electronics, and catalysis [19–22].

CNTs synthesis attempts to generate some high-temperature conditions straightforwardly on the situated material in a high-temperature range. Different synthesis methods were employed, including arc discharge [23], laser ablation [24], and several chemical vapor deposition forms (CVD) [25] give a wide range of approaches to yield CNTs. The CNTs manufacture via thermal method CVD (TCVD) is one of the most intriguing because of its capability to achieve enormous product amounts. Utilizing metal NPs as a nano-catalyst for TCVD is appealing because of the huge quantity of low-cost particles available and the weak concentrations of particles needed. Generally, the use of NPs is good for supplying a catalyst for the reaction of synthesis [26]. Due to the electrical conductivity of CNTs it can be present in both semiconducting and metallic phases that is connected to as a single or multi-wall. Furthermore, other aspects such as elasticity and strength help them to act as test tips for very high-resolution scanning microscopy. In contrast to numerous adsorbents, CNTs are beneficial because of advanced mesopores, considerable π - π electrostatic bonds, and large surface areas [27]. Besides, fitting the modification of CNTs could raise its surface functional groups, and create numerous open tubes by partially opening the end caps [28]. Ma and coworkers confirmed, for example, that alkali-activated multi-walled carbon nanotubes have the super capacity to remove not only methyl orange (149 mg/g) but also methylene blue (399 mg/g) [29,30].

The present study was undertaken to synthesize multiwalled carbon nanotubes modified by Cu and, or Zn individually or combined as a nanocomposites material as $\text{Cu}_{0.1}\text{Zn}_{0.9}\text{O}$ NPs. Characterization of the as-synthesized nanocomposites was carried out by XRD, N_2 physisorption, TEM, FT-IR, UV reflectance analysis, and Raman spectroscopy.

This work is aimed to study the photo-degradation of Congo red dye (CR) by utilizing the synthesized nanocomposites under visible light irradiation.

2. Experimental

2.1. Catalyst Preparation

Multi-walled carbon nanotubes were (supplied from EPRI nano-center) [31]. 5% Ni/MgO was prepared as follows: In a typical synthesis, the desired quantity of the $\text{Ni}(\text{NO}_3)_2 \cdot 6\text{H}_2\text{O}$ precursor (analytical reagent grades, Sigma–Aldrich) was dissolved inadequate amount of de-ionized water then added to the requisite amount of calcinated MgO support. Subsequently, the solution was stirred at ambient temperature for 1 h, followed by sonication for 10 min to obtain a homogenous slurry.

Finally, this slurry was dried at 120 °C for 12 h before calcination at 600 °C for 4 h in air. The process of growing CNTs operated using a fixed-bed horizontal-flow reactor (quartz, length= 100 cm, and diameter= 1.5 cm). Typically, 0.5 g of catalyst was employed in the center of the reactor and then condensed in-situ to the metallic energetic phase via 99.9% hydrogen at 700 °C for 1 h with a flow rate of 50 sccm (standard cubic centimeter per minute). Extraordinary purity methane (99.995%) with a flow rate of 50 sccm was accompanied at the surface of the catalyst below atmospheric pressure for decomposition trials. After the experiment, the reactor was cooled down to room temperature under N_2 flow of 100 $\text{cm}^3\text{min}^{-1}$. The obtained CNTs material has purity > 95% and its diameter 20-40 nm. The pure CNTs material was then impregnated with $\text{Cu}(\text{NO}_3)_2 \cdot 3\text{H}_2\text{O}$ and $\text{Zn}(\text{NO}_3)_2 \cdot 6\text{H}_2\text{O}$ to produce the monometallic 10 % CuO/CNT and 10% ZnO/CNT or the bimetallic 10% Cu-10% Zn/CNT catalyst. The catalyst was then dried at 100 °C and calcinated in the air at 250 °C for 4 h. The synthesized sample was denoted as CNT, Cu/CNT, Zn/CNT, and Cu-Zn/CNT

for the mother carbon nanotube, 20% Cu/CNT, 20% Zn/CNT, and 10% Cu-10% Zn/CNT, respectively.

2.2. Catalyst Characterization

X-ray diffraction (XRD) patterns were recorded on a Bruker AXS-D8 advanced X-ray using Cu-K α radiation ($\lambda = 1.5418 \text{ \AA}$) and scanning the 2θ angle from 10 to 70 degrees (scanning speed: 0.4 degrees/min). The average crystalline size, D_{XRD} , was calculated from Scherer's equation:

$D = 0.9\lambda / \beta \cos \theta$, where λ is the wavelength of X-ray radiation ($\lambda = 1.5418 \text{ \AA}$), β is the full peak width at half maximum (FWHM), and θ is the angle of diffraction. The surface area and pore volume of the solid materials were determined from N_2 adsorption isotherms measured at $-196 \text{ }^\circ\text{C}$ using a NOVA 3200 apparatus (Boynton Beach, FL, USA). The samples were initially out-gassed under vacuum (10^{-4} Torr) at $^\circ\text{C}$ for 24 h [32]. The accuracy in simulated isotherm curves exceeded 99.7%. Raman spectroscopy was performed at room temperature using SENTERRA Dispersive Raman Microscope (Bruker, Billerica, MA, USA) laser operating at a wavelength of 532 nm, with a spectrum range between 500 and 2000 cm^{-1} . The average particle sizes as well as the morphology of all samples being monitored using a High-resolution Electron microscope (HRTEM, (JEOL) JEM 2100, 120 Kw, 600,000 magnifications, Japan) attached with (EDX) Oxford X-Max. Scanning electron microscopy (SEM, ZEISS at 25 kV), FT-IR was used in the $4000\text{--}400 \text{ cm}^{-1}$ range recorded at room temperature by PerkinElmer (model spectrum, USA). Samples were prepared using the standard KBr pellets. The UV-reflectance analysis of the prepared materials was developed through a UV-spectrophotometer model V-570 manufactured by JASCO (Japan). The photoluminescence characteristics were determined at room temperature using a spectrofluorometer (JASCO FP-6500, Jasco International CO., Ltd., Tokyo, Japan) with an excitation wavelength set at $\lambda = 300 \text{ nm}$.

2.3. Photocatalytic Activity

The photocatalytic efficiency of the synthesized materials based on CNTs was tested for Congo red dye (CR) photocatalytic treatment. Photo-degradation was performed in a cylindrical reactor (quartz) batch system with a constant stirring of 250 rpm, and

aeration with an air bubble distributor ($1 \text{ dm}^3/\text{min}$) was acted at room temperature $25 \pm 1 \text{ }^\circ\text{C}$. A 100 mL of 25 mg/L dye solution contained 0.1 gm of nanoparticles and was kept in the dark for 30 minutes for adsorption balance. The suspension was then irradiated with one Tungsten visible lamp (250W, $\lambda_{\text{max}} = 400 \text{ nm}$). 5 mL of the samples were collected and centrifuged during irradiation periods. The degradation was checked by the aid of the absorbance calculations at $\lambda_{\text{max}} = 496 \text{ nm}$, UV-Visible Spectrometer (JASCO V-630), Japan.

3. Results and Discussion

3.1. XRD

Phase structures of all samples under this investigation are identified using X-ray analysis, demonstrated in Fig.1 (a & b). The mother (CNT) displays sharp peaks at 25.87° (002), 43.3° (110), and 53.9° (004) according to (ASTM card No. 00-058-1638), which related to multi-walled carbon nanotubes (MWCNTs), which had a graphitic like-structure [33]. Similar diffraction lines are observed in all studied catalysts. For the Cu/CNT sample, it is noticed that two peaks represented at 2θ of 35.49° (111) and 38.59° (002), which confirmed the existence of copper oxide phase (CuO) according to (ASTM card No. 00-041-0254). Sharp crystalline lines are detected in Zn/CNT sample, which appeared at 31.57° (100), 34.33° (002), 36.12° (101), 47.41° (102), 56.33° (110), 62.82° (103), and 67.73° (112) that ascribed to zinc oxide phase (ZnO) according to (ASTM card No. 00-005-0664) comparing all diffraction lines in the pattern of CuZn/CNT samples as illustrated in Fig.1. Their intensity was noticed because the polycrystalline phase was classified to each other. The diffraction lines appeared at 31.6° (100), 34.48° (002), 36.17° (101), 47.5° (102), 56.6° (110) and 62.93° (103), which related $\text{Cu}_{0.1}\text{Zn}_{0.9}\text{O}$ nanocomposite according to (ASTM card No. 04-019-3566) [34]. Also, peaks at 39.08° (100), 47.5° (102), 53.8° (004) which ascribed to Cu Zn alloy, which is related to Zhanghengite synthesis. Alternatively, the measured crystallite size of the mother CNTs was established to be 10.39 nm. The crystallite sizes of the CuO, ZnO, and $\text{Cu}_{0.1}\text{Zn}_{0.9}\text{O}$ loaded over pure CNT are higher than that of mother CNT, where it was 21.2 nm, 42.5 nm and 53.1 nm, respectively.

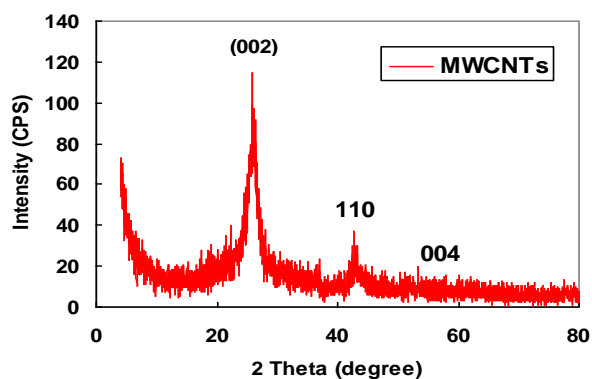


Figure 1a: XRD pattern of MWCNTs.

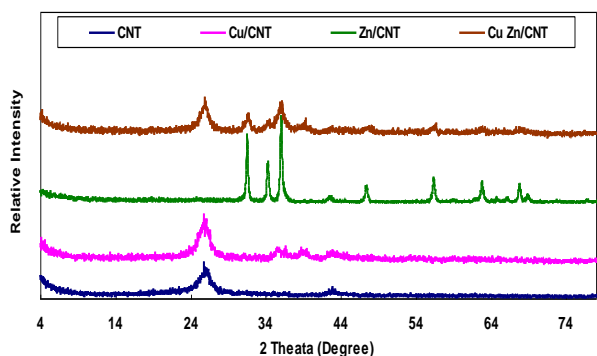


Figure 1b: XRD pattern of CNT and Cu and Zn supported samples.

3.2. Surface Area Measurement

N_2 adsorption-desorption of the mother CNTs and Cu/CNTs, Zn/CNTs, and the nanocomposites CuZn/CNTs catalyst samples are discussed in Fig. 2 and Table 1. All isotherms are similar to CNTs (the mother sample) and classified to kind II according to IUPAC types [35–39].

The N_2 was taken at minimal relative pressure P/P_0 , indicating the micropore filling from adsorbent-adsorbate interaction and is distinct from the adsorption in micropore multilayer, which ascribed to the multilayer adsorption. Both the surface area and the total pore volume of the mother CNTs were found to be $247 \text{ m}^2/\text{g}$ and $0.569 \text{ cm}^3/\text{g}$. The surface area of the metallic catalyst is decreased upon loading of the

Cu and Zn or both of them because of the incorporation of the metal particles inside the inner pores of CNTs or at the tube's tips. $\text{Cu}_{0.1}\text{Zn}_{0.9}\text{O}/\text{CNT}$ nanocomposite showed a higher surface area and total pore volume among common synthesized metal catalysts, which seemed to be $191 \text{ m}^2/\text{g}$ and $0.687 \text{ cm}^3/\text{g}$. PSD curve of the MWCNTs possesses a micropore that centered at 1.8 nm in addition to a wide mesopore, which centered at 30 nm, which can be assigned for the inner diameter of CNTs.

3.3. Raman Spectroscopy

Fig.3 shows the Raman spectra at room temperature of CNT and CuZn/CNT catalysts. The spectrum shows the G- band at $\sim 1570 \text{ cm}^{-1}$ it probably represents the expansion of all C-C pairs [40]. For the D band, a peak is detected at $\sim 1340 \text{ cm}^{-1}$; it probably represent convolution of C hexagonal rings [41,42], and for 2D band at $\sim 2670 \text{ cm}^{-1}$ resulted from double-resonance of the Raman procedure of [43,44]. They precisely attributed to graphene 7 crystalline. Also, at $\sim 1610 \text{ cm}^{-1}$, which identically assigned to the D-band, is a disorder-activated double-resonance Raman characteristic, and it is an ideal of mixed graphite and MWCNTs [45].

(I_D/I_G) intensities rate peaks of the D- and G-band is perfectly applied to adjust the defect density, and its reverse (I_G/I_D) is occupied as graphitization index for CNTs; on the other hand, (I_{2D}/I_G) , the intensities proportion peaks of 2D and G gives information about the elongated-range graphitic order [46].

The data explains that the CNT and CuZn/CNT samples have I_D/I_G close around 0.6 and 0.9, individually, which refers to a higher occurrence of a defect in the CuZn/CNT sample, so a reduced crystalline value. The I_{2D}/I_G data shows that (0.59 is for CNT) and (0.63 is for CuZn/CNT) [47].

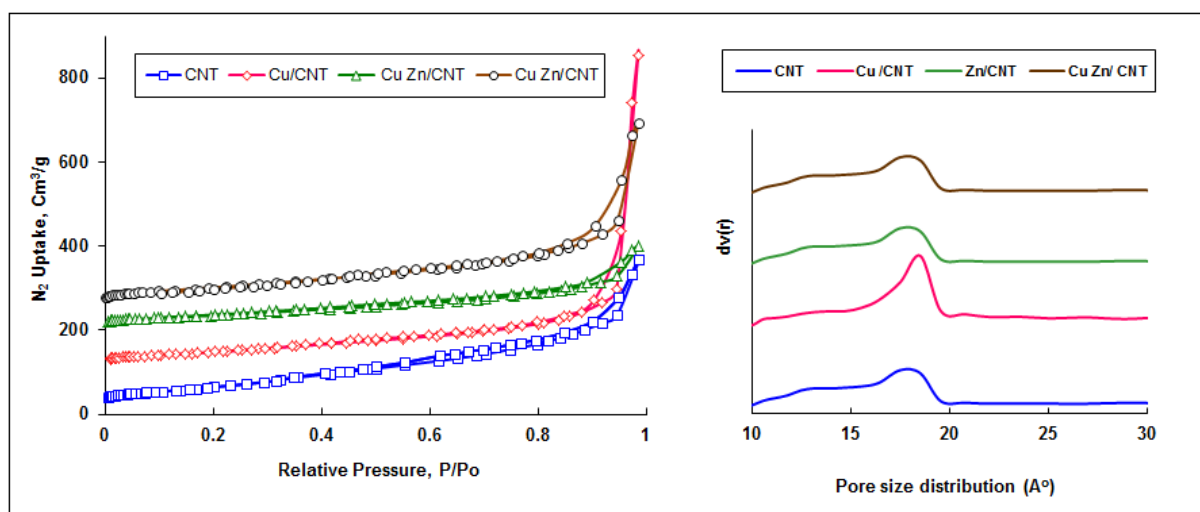


Figure 2: N₂ adsorption-desorption isotherm (a) and PSD curve (b) of the synthesized catalysts.

Table 1: Structural & texture characterizations of the synthesized catalysts.

Catalyst	FWHM (deg)	Grain Size (nm)	Microstrain	δ lines/ m ² x 10 ⁻³	S _{BET} (m ² /g)	V _p (cm ³ /g)	D _p (nm)
CNT	0.8640	10.39	0.211	9.26	247	0.569	9.21
CuO/CNT	0.4723	21.21	0.114	2.22	174	0.610	26.6
ZnO/CNT	0.2755	42.49	0.066	55.38	148	0.519	13.9
Cu _{0.1} Zn _{0.9} O/CNT	0.2362	53.11	0.056	35.45	191	0.687	14.4

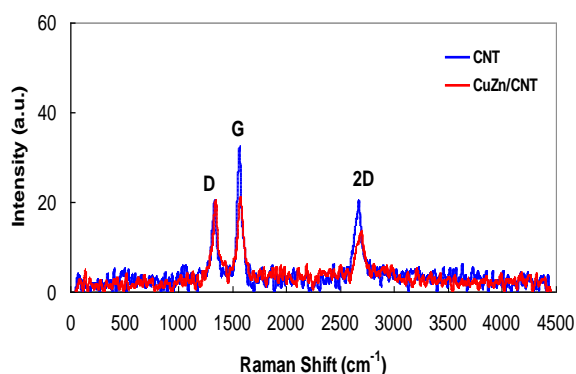


Figure 3: Raman spectra of CNT and CuZn/CNT catalysts.

3.4. TEM

Fig.4 showed TEM micrographs of the mother CNT, Cu/CNTs, Zn/CNTs, and Cu_{0.1}Zn_{0.9}O/CNTs. TEM results revealed that all samples are multi-walled carbon nanotubes. It is noted that Cu and Zn metals are located at the surface of CNTs. This trend depicted that both metals are distributed at random on

the catalysts' surface, resulting in variation in their average particle size. The dark parts in the pictures indicated that the metals are included at the tips of the tubes. Also, it indicated that the progress of the MWCNTs proceeds via the tip-growth mechanism. Fig.3b revealed that Cu metal in the Cu/CNTs catalyst sample exists at the surface and inside the tube, as evidenced by the tube dimensions' enlargement. It is seen that the Zn/CNTs have a homogeneously uniform diameter as compared to the bare CNTs. Also, Bimetallic Cu-Zn/CNTs seemed to have a uniform diameter, and both metals are existing at the surface of the nanotube and the tips of the tube via the tip-growth mechanism. The approximated average particle size of CuO and Cu_{0.1}Zn_{0.9} was found to be 24 and 55 nm, which runs in harmony with XRD results.

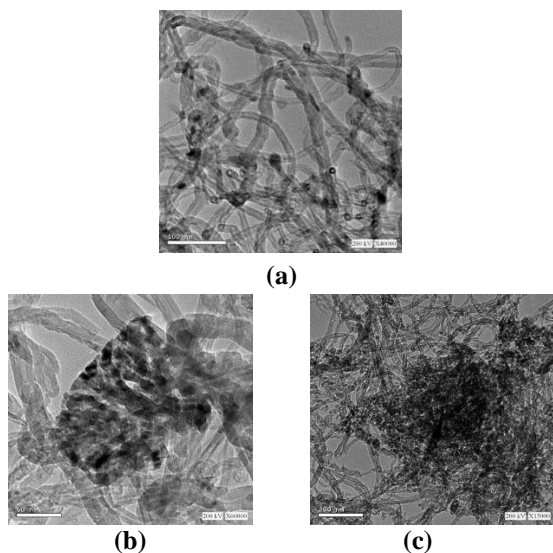


Figure 4: TEM micrographs of (a) CNT, (b) Cu/CNT, and (c) Cu-Zn/CNT catalyst samples.

3.5. FT-IR

Carbon nano-materials typically exhibit distinctive FT-IR absorptions based on their geometry and are very useful for carbon nano-material purity extents. FT-IR spectra were achieved within 400-4000 cm^{-1} under ordinary conditions. Fig.5 shows FT-IR of mother carbon nanotubes and CuO and ZnO supported catalysts. The entire samples exhibit identical vibrational bands, and the broad peak noticed at 3400 cm^{-1} is assigned to OH stretching vibration of hydroxyl groups and absorbed water [9,10] [48–50].

The peaks around 2910 and 2850 cm^{-1} of the samples appeared to be connected to CH_2 asymmetric vibration and CH_3 symmetric vibration, separately (Fig.5a). C-H stretching in aliphatic groups originates principally from groups of methyl and methylene bound to an aromatic group. The intensity of the peak at 2910 cm^{-1} is developed than that of the peak at 2850 cm^{-1} , which confirmed the existence of a long aliphatic chain in the mother carbon nanotube sample[12]. The peak at 1610 cm^{-1} of all samples is recognized to the C=C aromatic stretching vibration (G-band of graphite) [48], C = C Vinyl, and maybe because of other O-inclosing functional groups such as alcohol, phenols, carbonyls, ethers, and carboxylic acid. Broadband observed at approximately 1200 cm^{-1} is due to the carbon nano-composites presence, resulting from contributing the D-band of the FT-IR spectra of carbon nanocatalysts with defects. The

peak that appeared at around 1570 cm^{-1} is found to be because of the hexagonal C=C bond, which exists in multi-walled carbon nanotubes (Fig.5).

Zn/CNT catalysts showed intense peaks at 678 and 465 cm^{-1} which related to the stretching vibration of Zn-O bonds. It is well-known that the highly intense peak at 465 cm^{-1} doesn't notice in the IR spectrum of $\text{Cu}_{0.1}\text{Zn}_{0.9}\text{O}/\text{CNT}$ nanocomposite. This indicated that ZnO does not exist freely on the catalyst surface and this confirmed the solid solution formation between Cu/Zn. It is noticed that the used CNT sample and other supported metallic catalysts are not significantly affected by the adsorption of Congo red dye. The main function groups are completely maintained in the used catalysts.

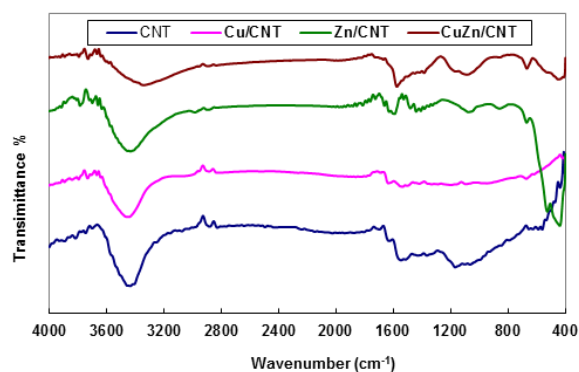


Figure 5: FT-IR of CNT, Cu/CNT, Zn/CNT, and CuZn/CNT catalyst samples.

3.6. SEM

SEM is considered a primary tool to characterize the surface morphology and fundamental physical properties of an adsorbent surface. It can be used for determining the particle shape, porosity, and particle size distribution of an adsorbent [51].

SEM micrographs of the mother CNT, Cu/CNTs, Zn/CNTs, and $\text{Cu}_{0.1}\text{Zn}_{0.9}\text{O}/\text{CNTs}$ were carried out by a scanning electron microscope (SEM ZEISS) and showed in Fig. 6. The SEM results confirmed the existence of multi-walled carbon nanotubes-based catalysts in all samples under this investigation. Fig.6b revealed that CuO particles are homogeneously coated on the surface of MWNTs and intimately attached to the MWNTs. It is also noticed that CuO nanoparticles are attached to the tip of MWNT which runs in harmony with the results collected from transmission electron microscope images [1], Fig.6c exhibited that the ZnO

nanoparticles were uniform in shape with a smooth surface and were incorporated into the surface of MWCNT [2].

It is seen that $\text{Cu}_{0.1}\text{Zn}_{0.9}\text{O}/\text{CNT}$ s nanocomposites appeared as agglomerated particles with the grains poorly observed in the analysis scale as illustrated in Fig. 6d. From the SEM images, we inferred that the NPs were regularly shaped and the crystallite structure was uniformly arranged on the surface. The compositions of the utilized catalysts (CuO/CNT , ZnO/CNT) were displayed and the signals corresponding to Zn or Cu, C, and O appeared with their relative intensity as shown in Figures 7a and 7b. In addition, no impurities were identified in the EDX spectrum. These results indicated that complete nanocrystals were formed with sufficient doping concentration and the distributions of Zn or Cu were observed in the loaded catalyst was about 25 and 28 %, respectively [3].

Moreover, the EDX spectrum of the synthesized nanocomposite sample (Fig. 7c) ensured the existence of the expected elements such as Zn, Cu, O, and CNTs in the given composite. The highly intense peak corresponding to the elemental C has been detected through the examined structure which emphasized the presence of the CNT in the structure of the sample. EDX represented that the suggested formula of the tested nanocomposite exists based on the wt% of the examined structure as instrumentally calculated.

3.7. Catalyst Photoluminescence (P.L.)

The ability of the material to promote photo-activated chemical reactions can also be documented by analyzing the photoluminescence of the sample. Fig. 8 shows the P.L. at room temperature of all samples with an excitation wavelength: $\lambda = 300$ nm. The major peak of luminescence appears at λ : 561 nm. This is in the red region of the light spectrum, consistently with the observations of optical absorption.

The electrons in the valence band move first to the conduction band, before being stabilized by the photo-emission. The P.L. intensity increases with increasing the number of emitted electrons resulting from the rapid recombination between excited electrons and holes, which, in turn, reduces the photo-activity of the catalyst. The wavelength of emission is directly correlated to the energy band-gap due to the recombination of a photo-generated hole

with an electron occupying the oxygen vacancy [52,53].

The P.L. intensity of the ZnO catalyst was very low compared to other catalysts. This means that the recombination of h^+ and e^- at the surface of the catalyst is slower, and then the catalytic activity is enhanced [54]. The direct comparison is made difficult by different excitation wavelengths; however, the difference in the order of magnitude is sufficient to demonstrate the activity of ZnO nanoparticles. This probably means that the recombination of h^+ and e^- is slow; this will undoubtedly affect the photocatalytic activity of ZnO nanoparticles.

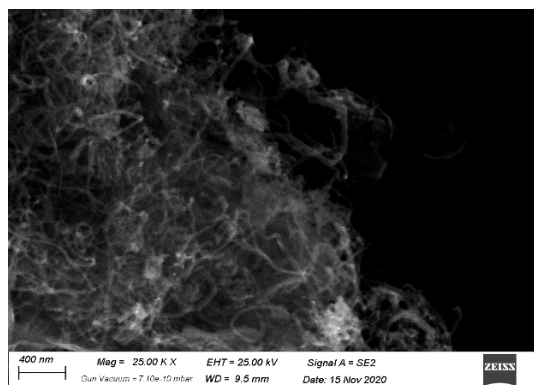
3.8. Optical Properties

The optical absorbance spectra of the parent carbon nanotube composite are represented in Fig. 9. All materials exhibited absorption bands within the visible area of the spectra. This is related to lowering the energy of the bandgap. The data was calculated from Tauc's equation [55].

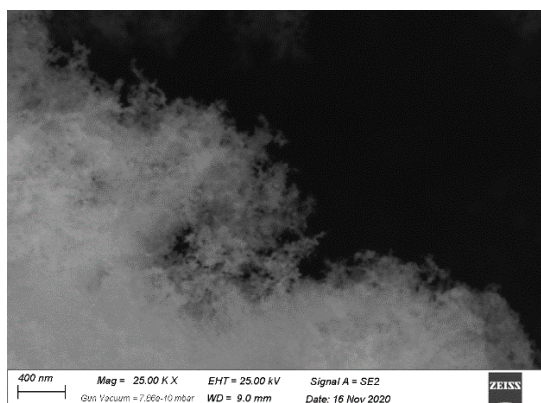
$$A = (h\nu - E_g)^{1/2} / h\nu$$

(α = absorption coefficient, A= sample absorbance, E_g = optical band gap, h = Planck's constant, ν = photon frequency.)

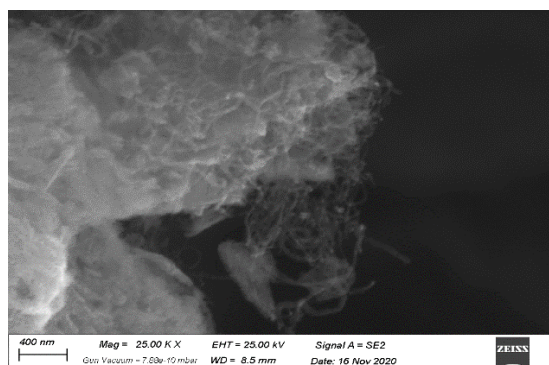
The bandgap value was calculated by generalizing the linear portion of $(\alpha h\nu)^2$ against $h\nu$ to intercept with the $h\nu$ axis as displayed in Figure 9. The figure shows the bandgap values are 2.46, 2.48, and 2.50 eV for Cu/CNT , Zn/CNT , and $\text{Cu-Zn}/\text{CNT}$ nanocomposite. The low bandgap energy low energy will need to exit the semiconductor electron from the ground state to the exciting state providing more electron/ hole pairs and enhancing the photoactivity. The decline of bandgap energy means speed excitation of electrons from the lowest unoccupied.



(b)

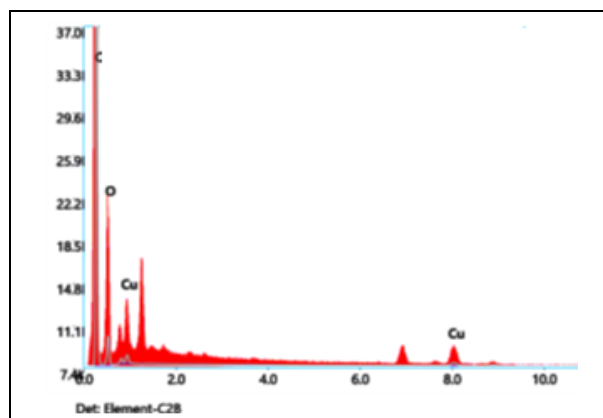


(c)

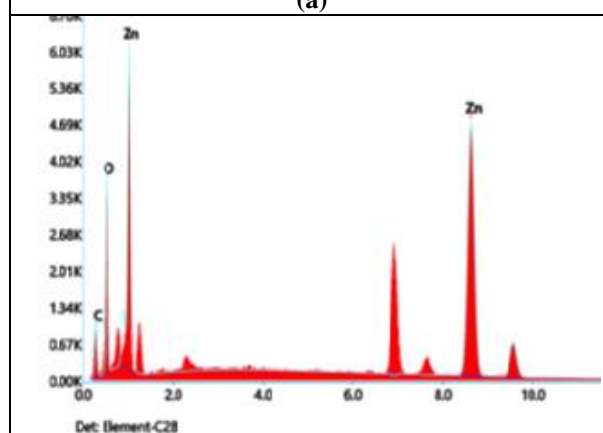


(d)

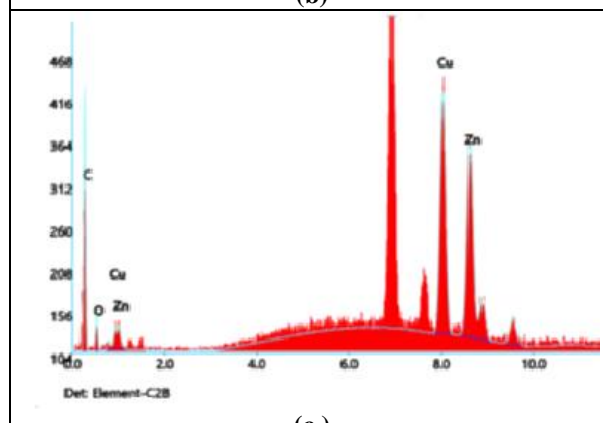
Figure 6: SEM micrographs of (a) CNT, (b) Cu/CNT (c)Zn/CNT and (d) Cu-Zn/CNT catalyst samples.



(a)



(b)



(c)

Figure 7: EDX spectrum of the same SEM spots.

molecular orbital to the highest occupied molecular orbital using low energy, which will provide more electron/positive hole pairs and increase the photocatalytic elimination of the dyes in the visible region [56].

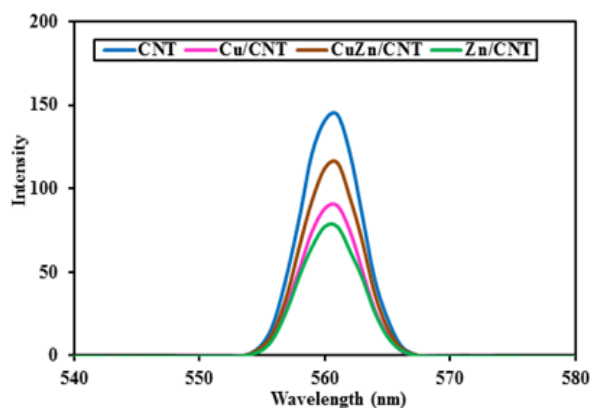


Figure 8: Photoluminescence spectrum of CNT, Cu/CNT, Zn/CNT, and CuZn/CNT catalyst samples (Room temperature; λ_{exc} : 300 nm).

3.9. Photocatalytic Activity

The catalytic-photo degradation tests of the CNT composites were achieved using Congo red dye (CR) under visible irradiation. Initially, the experiment was conducted in the dark for 60 minutes to reach the adsorption/desorption equilibrium [57].

Fig. 10 shows the degradation percent of dye utilizing only 0.1 g nanocomposites; the degradation efficiency increased gradually with rising irradiation time to 70 minutes at an initial dye concentration of 25 mg/L. The degradation efficiency is coincident with the adsorption affinity of the composite [58]; for example, the degradation efficiency increased from 89.2% to 92.9% to 97.7% using Cu-Zn/CNT, Cu/CNT, and Zn/CNT after 70 min under visible light. For Cu-Zn/CNT composite, 64.2% of degradation efficiency is related to adsorption, whereas, for Cu/CNT and Zn/CNT catalysts, 61.4% and 76.7% of the degradation is related to adsorption in the dark. In general, the as-prepared catalysts' photocatalytic activity is localized on many aspects like texture properties, bandgap energy, chemical structure, size, and the shape of the nano-materials composite, etc. Experimental conditions as irradiation time, operation parameters like pH solution, the catalyst's stability, and adsorption/desorption equilibrium onto the catalysts' surfaces.

In our study, the Zn/CNT composite shows the highest degradation efficiency among the prepared composites, irrespective of the low BET surface area. The Zn/CNT composite's photoactivity is related mainly to the high dislocation density value δ of 55.4,

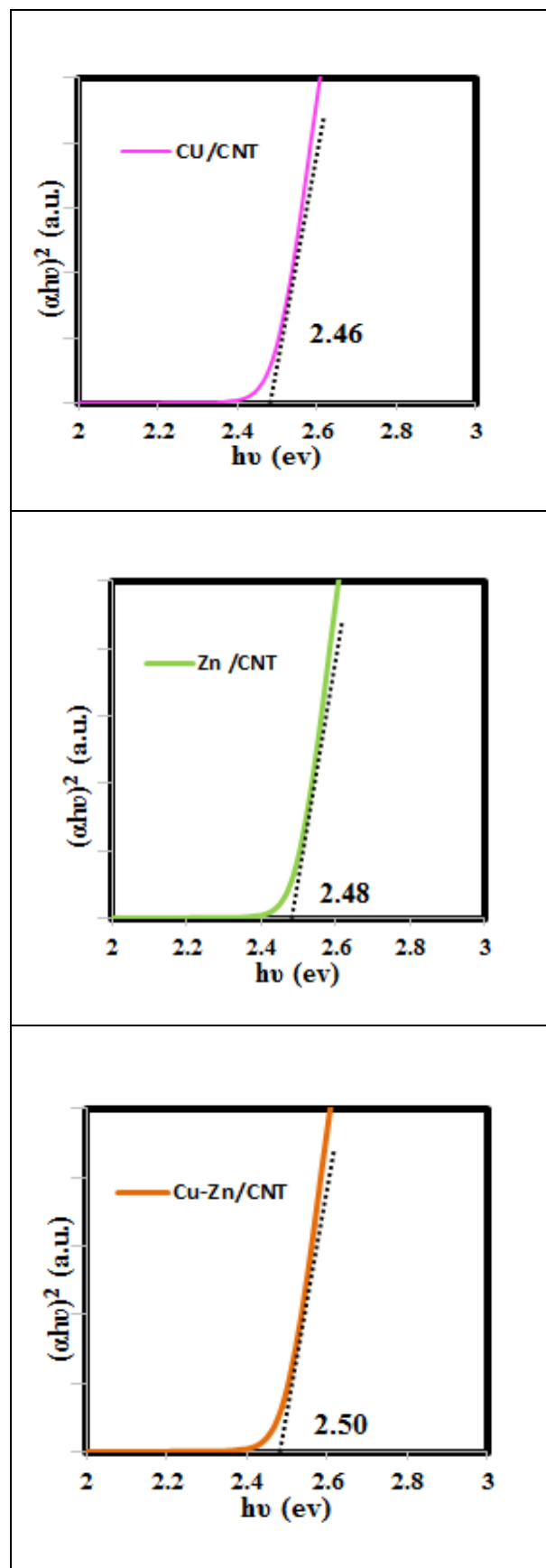


Figure 9: Energy band gaps of (a) Cu/CNT (b) Zn/CNT and (c) Cu-Zn/CNT catalyst samples.

representing the number of defects and vacancies in the crystal lattice. Lattice deficiency is a consequence created during the synthesis route and thermal- and preparation-dependent products [59].

Intrinsic point defects occur automatically in the lattice as vacancies, interstitials, and atomic impurities, commonly detected in doping materials. These defects may act like holes in active centers that depend on the growing photocatalytic activity. This result confirmed that the photoactivity is related mainly to the as-prepared composite's chemical structure, not texture one.

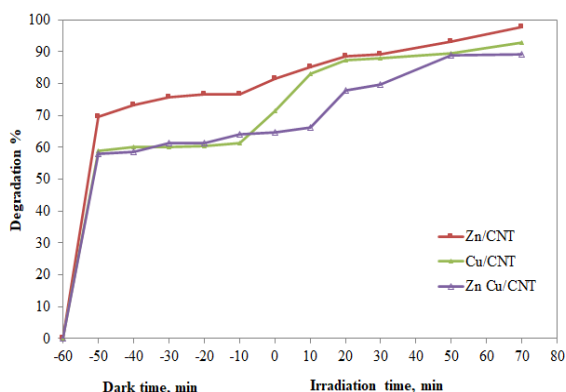


Figure 10. Photo-catalytic degradation of 25 ppm Congo red dye over Zn/CNT, Cu/CNT, and Zn-Cu/CNT composites using 1 gm/l catalyst dose under visible light.

The proposed mechanism could be inferred from the above results: if surface defect states occur, the electron or hole may be trapped, the recombination will be suppressed, and the oxidation-reduction rate may be increased. The broad defect populations were found in the ZnO/CNT sample. Many defects consist of robust band gap acceptor states that trap the holes and prevent recombination [60]. Various bands of defects facilitate the rate of separation of the electron-hole pair [61]. The enhanced photocatalytic efficiency is derived primarily from the large number of acceptor states caused by ZnO defects. In addition to expanding the light absorption edge of visible light, the acceptor states also delay the rate of recombination of electron-hole pairs. It believes that both large numbers of defects and acceptor states are responsible for improving photocatalytic performance. The presence of ZnO defects serves as an electron acceptor or a hole donor to promote the position of the carrier charges and thus prolonged

separation by trapping at energy levels close to the conductive or valence bands, respectively [62]. Photogenerated electrons (e_{cb}^-) can also react with electron acceptors such as O_2 adsorbed on the nanocomposite surface or dissolved in water, reducing it to radical anion $O_2^{\cdot-}$ superoxide. The photogenerated holes (h_{vb}^+) will react to oxidizing them into OH radicals by oxidizing them with OH^{\cdot} or H_2O . It is stated that the highly oxidizing species hydroxyl radicals (OH^{\cdot}), peroxide radicals (HO_2^{\cdot}), and superoxide radical anion $O_2^{\cdot-}$ are responsible for CR dye photodecomposition [58].

4. Conclusion

In this research work, multi-walled carbon nanotubes were prepared via chemical vapor synthesis (CVS). The mother CNTs were successfully modified by Cu and Zn (20% w/w) that loaded individually or combined together as nanocomposite structure $Cu_{0.1}Zn_{0.9}O$. The as-synthesized catalysts were examined in the photocatalytic degradation of Congo red dye under visible light irradiation. XRD results exhibited that the crystallinity of the mother CNTs was enhanced by introducing such metals under this investigation. The surface area of the Multi-walled CNT decreased upon loading of the Cu and Zn or their combined nanocomposite due to the incorporation of the metal particles inside the inner pores. The photocatalytic activity depicted that Zn/CNT composite shows the highest degradation efficiency among the prepared composites, which ascribed mainly to high dislocation density value δ of 55.4, representing the number of defects vacancies in the crystal lattice. This result confirmed that the photoactivity is related mainly to the prepared composite's chemical arrangement, not textural characterizations one.

References

- [1] T. Muñoz-Écija, B. Vargas-Quesada, and Z. Chinchilla Rodríguez, "Coping with methods for delineating emerging fields: Nanoscience and nanotechnology as a case study," *J. Informetr.*, vol. 13, no. 4, p. 100976, Nov. 2019, doi: 10.1016/j.joi.2019.100976.
- [2] J. Grunes, J. Zhu, and G. A. Somorjai, "Catalysis and nanoscience," *Chem. Commun.*, no. 18, p. 2257, 2003, doi: 10.1039/b305719b.
- [3] M. Moreno-Mañas and R. Pleixats, "Formation of Carbon-Carbon Bonds under Catalysis by

- Transition-Metal Nanoparticles,” *Acc. Chem. Res.*, vol. 36, no. 8, pp. 638–643, Aug. 2003, doi: 10.1021/ar020267y.
- [4] V. Mévellec, A. Roucoux, E. Ramirez, K. Philippot, and B. Chaudret, “Surfactant-Stabilized Aqueous Iridium(0) Colloidal Suspension: An Efficient Reusable Catalyst for Hydrogenation of Arenes in Biphasic Media,” *Adv. Synth. Catal.*, vol. 346, no. 1, pp. 72–76, Jan. 2004, doi: 10.1002/adsc.200303157.
- [5] I. Lisiecki and M. P. Pileni, “Synthesis of copper metallic clusters using reverse micelles as microreactors,” *J. Am. Chem. Soc.*, vol. 115, no. 10, pp. 3887–3896, May 1993, doi: 10.1021/ja00063a006.
- [6] R. S. Mohamed, A. A. Al Kahlawy, A. M. A. El Naggar, and H. M. Gobara, “Innovative approach for the production of carbon nanotubes (CNTs) and carbon nanosheets through highly efficient photocatalytic water splitting into hydrogen using metal organic framework (MOF)-nano TiO₂ matrices as novel catalysts,” *New J. Chem.*, p. 10.1039/C9NJ05422G, 2020, doi: 10.1039/C9NJ05422G.
- [7] R. A. Elsalamony and S. A. Mahmoud, “Preparation of nanostructured ruthenium doped titania for the photocatalytic degradation of 2-chlorophenol under visible light,” *Arab. J. Chem.*, vol. 10, no. 2, pp. 194–205, Feb. 2017, doi: 10.1016/j.arabj.2012.06.008.
- [8] R. A. Elsalamony and D. A. El-Hafiza, “Influence of Preparation Method on Copper Loaded Titania Nanoparticles: Textural, Structural Properties and Its Photocatalytic Activity towards P-Nitrophenol,” p. 14.
- [9] N. Sh. El-Gendy, R. A. El-Salamony, and S. A. Younis, “Green synthesis of fluorapatite from waste animal bones and the photo-catalytic degradation activity of a new ZnO/green biocatalyst nano-composite for removal of chlorophenols,” *J. Water Process Eng.*, vol. 12, pp. 8–19, Aug. 2016, doi: 10.1016/j.jwpe.2016.05.007.
- [10] R. A. El-Salamony, H. M. Gobara, S. A. Younis, and Y. M. Moustafa, “Zn²⁺-doped x-Ti-SiO₂ tricomposites for enhancement the photo-catalytic degradation of phenol under UV irradiation,” *J. Sol-Gel Sci. Technol.*, vol. 83, no. 2, pp. 422–435, Aug. 2017, doi: 10.1007/s10971-017-4427-7.
- [11] N. Mukwevho, E. Fosso-Kankeu, F. Waanders, N. Kumar, S. S. Ray, and X. Yangkou Mbianda, “Photocatalytic activity of Gd₂O₃·ZnO·CuO nanocomposite used for the degradation of phenanthrene,” *SN Appl. Sci.*, vol. 1, no. 1, p. 10, Jan. 2019, doi: 10.1007/s42452-018-0012-0.
- [12] Salah A. Hassan and Radwa A. El Salamony, “Photocatalytic Disc-Shaped Composite Systems for Removal of Hazardous Dyes in Aqueous Solutions,” *Can. Chem. Trans.*, pp. 57–71, 2014, doi: 10.13179/canchemtrans.2014.02.01.0057.
- [13] H. Gobara, R. El-Salamony, D. Mohamed, M. Mishrif, Y. Moustafa, and T. Gendy, “Use of SiO₂ - TiO₂ Nanocomposite as Photocatalyst for the Removal of Trichlorophenol: A Kinetic Study and Numerical Evaluation,” p. 20.
- [14] R. E. Morsi and R. A. Elsalamony, “Superabsorbent enhanced-catalytic core/shell nanocomposites hydrogels for efficient water decolorization,” *New J. Chem.*, vol. 40, no. 3, pp. 2927–2934, 2016, doi: 10.1039/C5NJ02823J.
- [15] R. A. El-Salamony, A. A. Emam, N. A. Badawy, and S. F. El-Morsi, “Photo-catalytic Study of Malachite Green Dye Degradation using Rice Straw Extracted Activated Carbon Supported ZnO nano-particles,” *Nanosci. Nanotechnol.-Asia*, vol. 09, Jul. 2019, doi: 10.2174/2210681209666190722121926.
- [16] R. A. El-Salamony and S. A. Hassan, “Reforming of Rice Ash Waste by Incorporated Nanotitania in Silica Framework for Photocatalytic Treatment of Wastewater,” *Appl. Organomet. Chem.*, Jun. 2020, doi: 10.1002/aoc.5824.
- [17] “Kroto H W, Heath J R, O’Brien S C, Curl R F & Smalley R E. C: buckminsterfullerene. *Nature* 318:162-3, 1985.” p. 2.
- [18] M. Monthieux and V. L. Kuznetsov, “Who should be given the credit for the discovery of carbon nanotubes?,” *Carbon*, vol. 44, no. 9, pp. 1621–1623, Aug. 2006, doi: 10.1016/j.carbon.2006.03.019.
- [19] T. Das, B. K. Saikia, and B. P. Baruah, “Formation of carbon nano-balls and carbon nano-tubes from northeast Indian Tertiary coal: Value added products from low grade coal,” *Gondwana Res.*, vol. 31, pp. 295–304, Mar. 2016, doi: 10.1016/j.gr.2015.01.012.
- [20] A. Dosodia, C. Lal*, B. P. Singh, R. B. Mathur, and D. K. Sharma*, “Development of Catalyst Free Carbon Nanotubes from Coal and Waste Plastics,” *Fuller. Nanotub. Carbon Nanostructures*, vol. 17, no. 5, pp. 567–582, Oct. 2009, doi: 10.1080/15363830903133238.
- [21] J. Yu, J. Lucas, V. Strezov, and T. Wall, “Coal and carbon nanotube production,” *Fuel*, vol. 82, no. 15–17, pp. 2025–2032, Oct. 2003, doi: 10.1016/S0016-2361(03)00189-3.
- [22] M. A. M. Ali, A. M. Alsabagh, M. W. Sabaa, R. A. El-Salamony, R. R. Mohamed, and R. E. Morsi, “Polyacrylamide hybrid nanocomposites hydrogels for efficient water treatment,” *Iran. Polym. J.*, vol. 29, no. 6, pp. 455–466, Jun. 2020, doi: 10.1007/s13726-020-00810-y.
- [23] Y. Saito, T. Nakahira, and S. Uemura, “Growth Conditions of Double-Walled Carbon Nanotubes

- in Arc Discharge,” *J. Phys. Chem. B*, vol. 107, no. 4, pp. 931–934, Jan. 2003, doi: 10.1021/jp021367o.
- [24] A. Thess *et al.*, “Crystalline Ropes of Metallic Carbon Nanotubes,” *Science*, vol. 273, no. 5274, pp. 483–487, Jul. 1996, doi: 10.1126/science.273.5274.483.
- [25] C. J. Lee, J. H. Park, and J. Park, “Synthesis of bamboo-shaped multiwalled carbon nanotubes using thermal chemical vapor deposition,” *Chem. Phys. Lett.*, vol. 323, no. 5–6, pp. 560–565, Jun. 2000, doi: 10.1016/S0009-2614(00)00548-0.
- [26] H. Ago, K. Nakamura, S. Imamura, and M. Tsuji, “Growth of double-wall carbon nanotubes with diameter-controlled iron oxide nanoparticles supported on MgO,” *Chem. Phys. Lett.*, vol. 391, no. 4–6, pp. 308–313, Jun. 2004, doi: 10.1016/j.cplett.2004.04.110.
- [27] Y. Zhang *et al.*, “Kinetics and Interfacial Thermodynamics of the pH-Related Sorption of Tetrabromobisphenol A onto Multiwalled Carbon Nanotubes,” *ACS Appl. Mater. Interfaces*, vol. 6, no. 23, pp. 20968–20977, Dec. 2014, doi: 10.1021/am505730f.
- [28] H. Li, D. Zhang, X. Han, and B. Xing, “Adsorption of antibiotic ciprofloxacin on carbon nanotubes: pH dependence and thermodynamics,” *Chemosphere*, vol. 95, pp. 150–155, Jan. 2014, doi: 10.1016/j.chemosphere.2013.08.053.
- [29] J. Ma, Fei Yu, Lu Zhou, *et al.*, “Enhanced Adsorptive Removal of Methyl Orange and Methylene Blue from Aqueous Solution by Alkali-Activated Multiwalled Carbon Nanotubes,” *ACS Appl. Mater. Interfaces*, vol. 4, no. 11, pp. 5749–5760, Nov. 2012, doi: 10.1021/am301053m.
- [30] O. I. Zelenskii, V. M. Shmal’ko, V. G. Udovitskii, and A. Yu. Kropotov, “Production of carbon nanostructures by the atomization of solid coking products within an electric arc,” *Coke Chem.*, vol. 55, no. 2, pp. 76–81, Feb. 2012, doi: 10.3103/S1068364X1202010X.
- [31] W. Ahmed, M. R. Noor El-Din, A. A. Aboul-Enein, and A. E. Awadallah, “Effect of textural properties of alumina support on the catalytic performance of Ni/Al₂O₃ catalysts for hydrogen production via methane decomposition,” *J. Nat. Gas Sci. Eng.*, vol. 25, pp. 359–366, Jul. 2015, doi: 10.1016/j.jngse.2015.05.015.
- [32] H. M. Gobara, I. M. Nassar, A. M. A. El Naggar, and Gh. Eshaq, “Nanocrystalline spinel ferrite for an enriched production of hydrogen through a solar energy stimulated water splitting process,” *Energy*, vol. 118, pp. 1234–1242, Jan. 2017, doi: 10.1016/j.energy.2016.11.001.
- [33] Q. Wen, Y. Wang, K. Xu, N. Li, H. Zhang, and Q. Yang, “A novel polymeric ionic liquid-coated magnetic multiwalled carbon nanotubes for the solid-phase extraction of Cu, Zn-superoxide dismutase,” *Anal. Chim. Acta*, vol. 939, pp. 54–63, Oct. 2016, doi: 10.1016/j.aca.2016.08.028.
- [34] D. Saravanakumar *et al.*, “Synthesis and characterization of CuO/ZnO/CNTs thin films on copper substrate and its photocatalytic applications,” *OpenNano*, vol. 4, p. 100025, 2019, doi: 10.1016/j.onano.2018.11.001.
- [35] S. A. Hassan, A. S. Darwish, H. M. Gobara, N. E. A. Abed-elsatar, and S. R. Fouda, “Interaction profiles in poly (amidoamine) dendrimer/montmorillonite or rice straw ash hybrids-immobilized magnetite nanoparticles governing their removal efficiencies of various pollutants in wastewater,” *J. Mol. Liq.*, vol. 230, pp. 353–369, Mar. 2017, doi: 10.1016/j.molliq.2017.01.060.
- [36] M. S. Ghattas, H. M. Gobara, S. A. Henin, S. A. Hassan, and F. H. Khalil, “Role of Structure and Acidic Nature on Catalytic Behavior of Nickel Supported H-mordenite, H-ZSM-5, and γ -alumina Catalysts,” *Pet. Sci. Technol.*, vol. 25, no. 10, pp. 1279–1291, Oct. 2007, doi: 10.1080/10916460600803645.
- [37] H. M. Gobara and S. A. Hassan, “A Comparative Study of Surface Characteristics of Nickel Supported on Silica Gel, γ -Alumina, Aluminosilicate,” *Pet. Sci. Technol.*, vol. 27, no. 14, pp. 1555–1571, Oct. 2009, doi: 10.1080/10916460802608677.
- [38] H. M. Salem, R. S. Mohamed, A. A. Alkahlawy, H. M. Gobara, A. E. A. Hassan, and S. A. Hassan, “Enhanced ethylene production by dehydration of ethanol over Al/SBA-15 mesoporous catalysts,” *J. Porous Mater.*, vol. 26, no. 3, pp. 735–745, Jun. 2019, doi: 10.1007/s10934-018-0670-8.
- [39] H. M. Gobara, R. S. Mohamed, S. A. Hassan, F. H. Khalil, and M. S. El-Sall, “Pt and Ni Nanoparticles Anchored into Metal–Organic Frameworks MIL-101 (Cr) as Swift Catalysts for Ethanol Dehydration,” *Catal. Lett.*, vol. 146, no. 10, pp. 1875–1885, Oct. 2016, doi: 10.1007/s10562-016-1826-2.
- [40] A. C. Ferrari and J. Robertson, “Interpretation of Raman spectra of disordered and amorphous carbon,” *Phys. Rev. B*, vol. 61, no. 20, pp. 14095–14107, May 2000, doi: 10.1103/PhysRevB.61.14095.
- [41] H. Kuzmany, B. Burger, A. Thess, and R. E. Smalley, “Vibrational spectra of single wall carbon nanotubes,” *Carbon*, vol. 36, no. 5–6, pp. 709–712, 1998, doi: 10.1016/S0008-6223(98)00071-2.

- [42] M. S. Dresselhaus, G. Dresselhaus, R. Saito, and A. Jorio, "Raman spectroscopy of carbon nanotubes," *Phys. Rep.*, vol. 409, no. 2, pp. 47–99, Mar. 2005, doi: 10.1016/j.physrep.2004.10.006.
- [43] A. C. Ferrari *et al.*, "Raman Spectrum of Graphene and Graphene Layers," *Phys. Rev. Lett.*, vol. 97, no. 18, p. 187401, Oct. 2006, doi: 10.1103/PhysRevLett.97.187401.
- [44] L. M. Malard, M. A. Pimenta, G. Dresselhaus, and M. S. Dresselhaus, "Raman spectroscopy in graphene," *Phys. Rep.*, vol. 473, no. 5–6, pp. 51–87, Apr. 2009, doi: 10.1016/j.physrep.2009.02.003.
- [45] S. Lee, J.-W. Peng, and C.-H. Liu, "Probing plasma-induced defect formation and oxidation in carbon nanotubes by Raman dispersion spectroscopy," *Carbon*, vol. 47, no. 15, pp. 3488–3497, Dec. 2009, doi: 10.1016/j.carbon.2009.08.019.
- [46] Y. A. Kim, T. Hayashi, K. Osawa, M. S. Dresselhaus, and M. Endo, "Annealing effect on disordered multi-wall carbon nanotubes," *Chem. Phys. Lett.*, vol. 380, no. 3–4, pp. 319–324, Oct. 2003, doi: 10.1016/j.cpllett.2003.09.027.
- [47] V. Loise *et al.*, "The effect of multiwalled carbon nanotubes on the rheological behaviour of bitumen," *Colloids Surf. Physicochem. Eng. Asp.*, vol. 566, pp. 113–119, Apr. 2019, doi: 10.1016/j.colsurfa.2019.01.021.
- [48] R. S. Mohamed, A. A. Al Kahlawy, A. M. A. El Naggar, and H. M. Gobara, "Innovative approach for the production of carbon nanotubes (CNTs) and carbon nanosheets through highly efficient photocatalytic water splitting into hydrogen using metal organic framework (MOF)-nano TiO₂ matrices as novel catalysts," *New J. Chem.*, p. 10.1039/C9NJ05422G, 2020, doi: 10.1039/C9NJ05422G.
- [49] H. M. Gobara, "Characterization and catalytic activity of NiO/mesoporous aluminosilicate AISBA-15 in conversion of some hydrocarbons," *Egypt. J. Pet.*, vol. 21, no. 1, pp. 1–10, Jun. 2012, doi: 10.1016/j.ejpe.2012.02.001.
- [50] Asmaa E. Elsayed, Doaa I. Osman, Sayed K. Attia, Hayam M. Ahmed, Eman M. Shoukry, Yasser M. Mostafa and Afaf R. Taman, "A study on the removal characteristics of organic and inorganic pollutants from wastewater by low cost biosorbent," *Egypt. J. Chem.*, vol. 63, no. 4, pp. 1429–1442, 2020, doi: 10.21608/ejchem.2019.15710.1950.
- [51] M. A. Diab, M. I. ElGammal, M. S. Ibrahim, G. A. Mahmoud, S. Sorour, and Sh. Rezoka, "Synthesis and characteristic of CMC/AM/PAC polymer for natural organic matter and Trihalomethanes removal from water," *Egypt. J. Chem.*, vol. 62, no. 1, pp. 279–291, Jun. 2019, doi: 10.21608/ejchem.2019.11688.1744.
- [52] A. S. Morshedy, Sahar M. Tawfik, Karam M. Hashem, *et al.*, "The production of clean diesel fuel by facile sun light photocatalytic desulfurization process using Cd-based diacetate as a novel liquid photocatalyst," *J. Clean. Prod.*, vol. 279, p. 123629, Jan. 2021, doi: 10.1016/j.jclepro.2020.123629.
- [53] H. A. Elwan, A. S. Morshedy, and A. M. A. El Naggar, "Highly Efficient Visible-Light-Induced Photocatalytic Hydrogen Production via Water Splitting using FeCl₃-Based Ionic Liquids as Homogeneous Photocatalysts," *ChemSusChem*, p. cssc.202001773, Oct. 2020, doi: 10.1002/cssc.202001773.
- [54] A. S. Morshedy, Ahmed M.A. El Naggar, Sahar M. Tawfik *et al.*, "Preparation and Characterization of Micro-Porous ZnO Nanoparticles," *Egypt. J. Chem.*, vol. 59, no. 4, pp. 609–621, Aug. 2016, doi: 10.21608/ejchem.2016.2339.
- [55] R. A. El-Salamony, E. Amdeha, N. A. Badawy, S. A. Ghoneim, and A. M. Al-Sabagh, "Visible light sensitive activated carbon-metal oxide (TiO₂, WO₃, NiO, and SnO) nano-catalysts for photo-degradation of methylene blue: a comparative study," *Toxicol. Environ. Chem.*, vol. 100, no. 2, pp. 143–156, Feb. 2018, doi: 10.1080/02772248.2018.1497634.
- [56] R. A. El-Salamony, E. Amdeha, S. A. Ghoneim, N. A. Badawy, K. M. Salem, and A. M. Al-Sabagh, "Titania modified activated carbon prepared from sugarcane bagasse: adsorption and photocatalytic degradation of methylene blue under visible light irradiation," *Environ. Technol.*, vol. 38, no. 24, pp. 3122–3136, Dec. 2017, doi: 10.1080/21622515.2017.1290148.
- [57] N. H. Shalaby, R. A. Elsalamony, and A. M. A. El Naggar, "Mesoporous waste-extracted SiO₂ – Al₂O₃-supported Ni and Ni–H₃PW₁₂O₄₀ nano-catalysts for photo-degradation of methyl orange dye under UV irradiation," *New J. Chem.*, vol. 42, no. 11, pp. 9177–9186, 2018, doi: 10.1039/C8NJ01479E.
- [58] W. A. Aboutaleb and R. A. El-Salamony, "Effect of Fe₂O₃-CeO₂ nanocomposite synthesis method on the Congo red dye photodegradation under visible light irradiation," *Mater. Chem. Phys.*, vol. 236, p. 121724, Oct. 2019, doi: 10.1016/j.matchemphys.2019.121724.
- [59] D. Levis and L. F. Cugliandolo, "Defects dynamics following thermal quenches in square spin ice," *Phys. Rev. B*, vol. 87, no. 21, p. 214302, Jun. 2013, doi: 10.1103/PhysRevB.87.214302.
- [60] L.-C. Tien, W.-T. Chen, and C.-H. Ho, "Enhanced Photocatalytic Activity in β -Ga₂O₃ Nanobelts: Enhanced Photocatalytic Activity in β -

-
- Ga₂O₃ Nanobelts,” *J. Am. Ceram. Soc.*, vol. 94, no. 9, pp. 3117–3122, Sep. 2011, doi: 10.1111/j.1551-2916.2011.04479.x.
- [61] C.-H. Ho, C.-Y. Tseng, and L.-C. Tien, “Thermoreflectance characterization of β -Ga₂O₃ thin-film nanostrips,” *Opt. Express*, vol. 18, no. 16, p. 16360, Aug. 2010, doi: 10.1364/OE.18.016360.
- [62] E. Ra, “Advances in Photo-catalytic Materials for Environmental Applications,” *Res. Rev. J. Mater. Sci.*, vol. 04, no. 02, 2016, doi: 10.4172/2321-6212.1000145.